Chapter 2

Ultra-high Q microtoroid

2.1 Microtoroid resonator overview

The silica microtoroid is an ultra-high Q (UHQ) and ultra-small mode volume microcavity fabricated on silicon using standard microelectronics techniques. Although silica microspheres have shown higher quality factors than microtoroids (8×10^9 compared to 5×10^8), their geometry and fabrication method present practical limitations [32]. The physical dimensions of a microsphere are difficult to control during melting, since there is no physical stop for the surface-tension induced reflow. Secondly, the microsphere's mode spectrum is more dense and complicated than the microtoroid, because the optical mode is not restricted in azimuthal and vertical degrees of freedom as the microtoroid is [33]. These challenges, and lack of planar integration of the microsphere in a compact package, led to the invention of the microtoroid [10]. The microtoroid is the first microcavity that offers ultra-high quality factor on silicon. The highest Q factor recorded in a microtoroid to date is 4×10^8, which corresponds to a cavity finesse ($F = \frac{\lambda Q}{\pi n D}$) of 1×10^6. Also, the microtoroid's cavity dimensions can be accurately controlled during fabrication to produce the desired resonator. For instance, small diameter toroids are needed for cQED experiments, where as larger toroids are important for laser operation in water.

A SEM image of a typical silica microtoroid is shown in Figure 2.1, with 60 μm major diameter (D) and 5 μm minor diameter (d). After fabrication, the microtoroid can be described as a glass ring cavity with a dumbbell-like cross section, suspended over a silicon pillar by a silica membrane. In microtoroids, like optical fiber and microspheres, the silica is amorphous. Alternatively, crystalline quartz rods have been carefully polished into WGM resonators with ultra-high Q (5×10^9) [34]. The advantage of amorphous silica is that it can easily be melted or drawn into the desire shape, though care should be taken not to freeze significant refractive index variations in the glass that cause scattering loss. Input light, for example from a fiber taper, orbits the microtoroid confined by TIR until it is absorbed, scattered out, or coupled out by another waveguide.
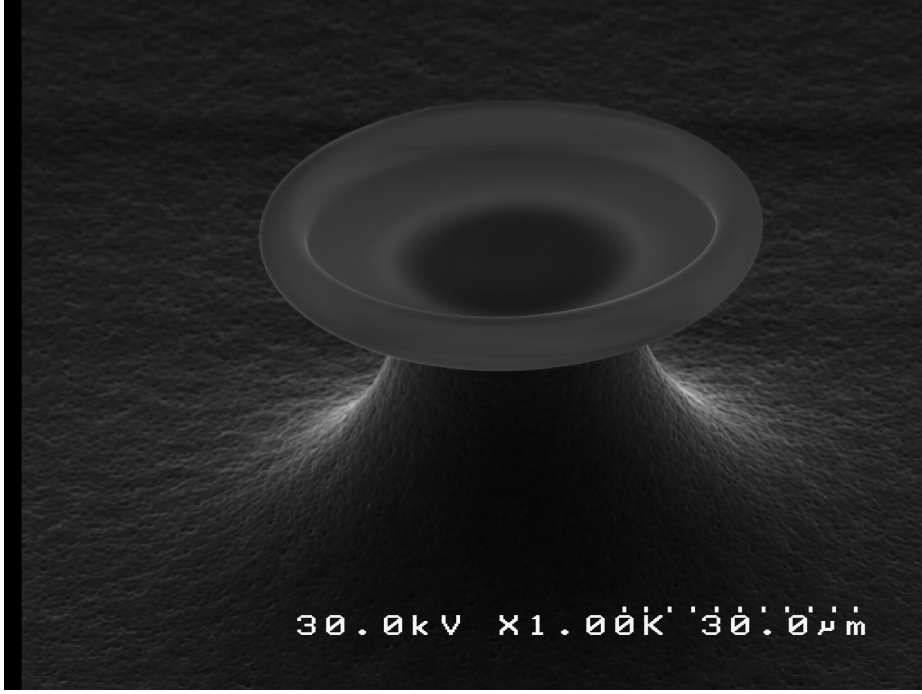
Figure 2.1. SEM image of a UHQ microtoroid resonator with 60 μm major diameter (D) and 5 μm minor diameter (d)

2.1.1 Whispering-gallery mode structure

The spatial confinement of microtoroids supports less transverse and radial modes than microspheres. These are whispering-gallery modes, so named because the photons circulate at the surface of the glass microcavity in a similar manner as sound waves do around the dome in St. Paul's Cathedral in London. Unlike the complete theory developed for microspheres, analytical expressions for the microtoroid mode structure are not possible because only one coordinate of the wave equation is separable. Therefore, the two-dimensional Helmholtz equation must be solved numerically, or by semi-analytical methods [35]. Sean Spillane developed a model of the 2D cross section of the microtoroid including rotational symmetry using a finite element eigenmode solver (Femlab). This full-vectorial model gives accurate solutions of the toroid's electromagnetic field distribution. The model can also calculate cavity mode volume, radiation Q, and resonance wavelengths. Figure 2.2 is a cross-sectional plot of two microtoroid cavity modes.
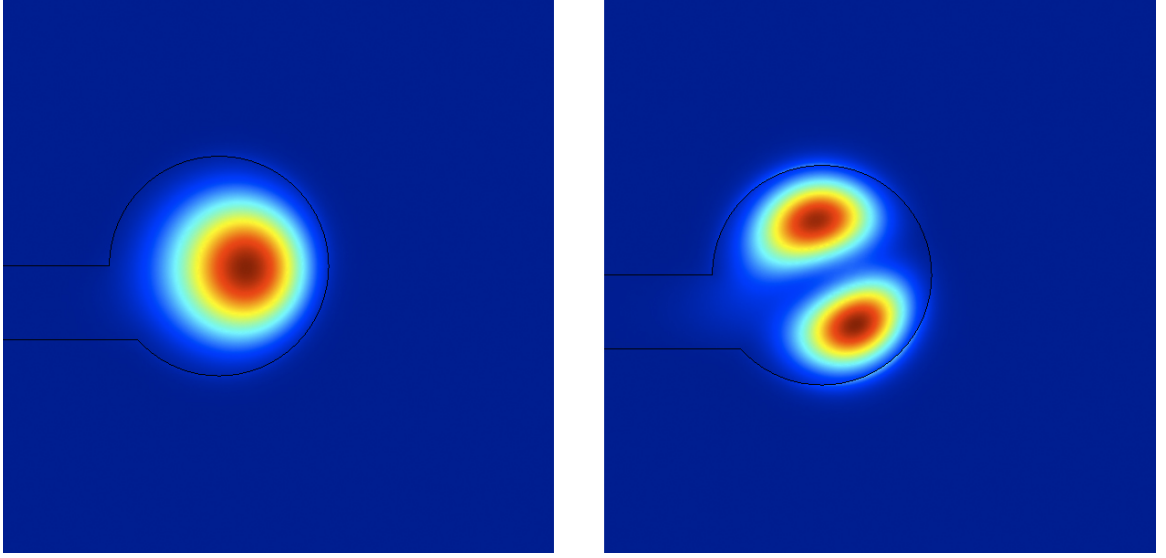
Figure 2.2. Plot of the electric field intensity profile $|E_\phi|^2$ of a 120 μm diameter toroid, showing the fundamental mode (left) and a higher-order mode (right). The field profiles are calculated by a FEM simulation of the microtoroid

To give a theoretical overview of the microtoroid cavity, the equations describing the microtoroid's mode structure are briefly detailed. To determine the proper description, start with Maxwell's equations in an isotropic charge free medium following Yariv [36].

$$\nabla \times \mathbf{H} = \varepsilon \frac{\partial \mathbf{E}}{\partial t} \tag{2.1}$$

$$\nabla \times \mathbf{E} = -\mu \frac{\partial \mathbf{H}}{\partial t} \tag{2.2}$$

$$\nabla \cdot (\varepsilon \mathbf{E}) = 0 \tag{2.3}$$

After taking the curl of Equation (2.2) and substitution, the expression becomes

$$\nabla^2 \mathbf{E} - \mu\varepsilon \frac{\partial^2 \mathbf{E}}{\partial t^2} = -\nabla(\frac{1}{\varepsilon}\mathbf{E} \cdot \nabla\varepsilon) \tag{2.4}$$

Next, write the field components $(H_r, H_\phi, H_z, E_r, E_\phi, E_z)$ in cylindrical coordinates, which is logical because of the microtoroid's rotational symmetry. For instance, the electric field $\mathbf{E}$ is written

$$\mathbf{E}(r, \phi, z, t) = \mathrm{Re}[\mathbf{E}(r, \phi, z)e^{iwt}] \tag{2.5}$$

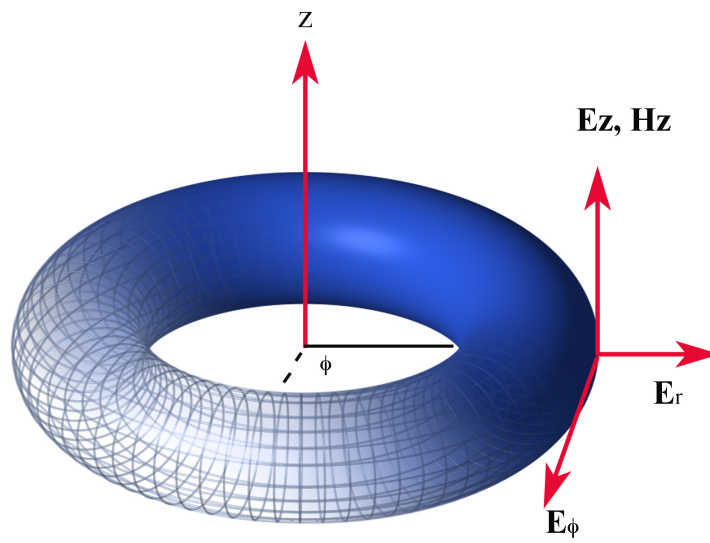The coordinate axis with respect to the toroid are shown in Figure 2.3.

Figure 2.3. Diagram of a toroid with field components in cylindrical coordinates for the TM-type whispering-gallery modes

Next, set the right side of Equation (2.2) equal to zero, since the permittivity of the medium is constant over one wavelength. After taking the double partial differential of $\mathbf{E}$, one produces the famous wave equation:

$$(\nabla^2 + \mu\varepsilon w^2)\mathbf{E} = 0 \tag{2.6}$$

Now, the scalar wave equation approximation can be applied because the refractive index is constant over a wavelength in the microtoroid, and the whispering-gallery mode polarization is preserved. Also, apply the substitution of $\mu\varepsilon = \mu_0\varepsilon_0 n^2 = n^2/c^2$. The resulting expression is the scalar wave equation for propagation in a dielectric medium, also known as the Helmholtz equation.

$$(\nabla^2 + \frac{w^2 n^2}{c^2})E = 0 \tag{2.7}$$

The microtoroid modes, solutions to Equation (2.7), have either transverse-electric (TE) or transverse-magnetic (TM) polarization in the cavity. In TE modes, the electric field oscillates in the (r, z) plane, transverse to the propagation direction (along ϕ), and hence $E_\phi = 0$. Likewise, in TM modes the magnetic field oscillates in the (r, z) plane and $H_\phi = 0$. The four remaining field components can be expressed with two field components ($H\phi$ for TE modes, and $E\phi$ for TM modes). After expanding the Laplacian operator, the scalar wave equation in terms of E_ϕ is

$$\left[\frac{\partial^2}{\partial r^2} + \frac{\partial}{r\partial r} + \frac{\partial^2}{r^2\partial\phi^2} + \frac{\partial^2}{\partial z^2} + \frac{w^2 n^2}{c^2} \right] E_\phi = 0 \tag{2.8}$$

Next, separate variables and express the electric field as $E_\phi = E_\phi(r, z)e^{(\pm il\phi)}$, where l is the angular mode number.

$$\left[\frac{\partial^2}{\partial r^2} + \frac{\partial}{r\partial r} - \frac{l^2}{r^2} + \frac{\partial^2}{\partial z^2} + \frac{w^2 n^2}{c^2} \right] E_\phi(r, z) = 0 \tag{2.9}$$

After arranging the terms, one reaches the Helmholtz equation in partial differential format.

$$\left(\frac{\partial}{\partial r} \frac{1}{r} \frac{\partial}{\partial r} + r\frac{\partial^2}{\partial z^2} \right) E_\phi + \left(\frac{w^2 n^2}{c^2} - \frac{l^2}{r^2} \right) rE_\phi = 0 \tag{2.10}$$

The whispering-gallery mode profiles can be calculated by using a FEM solver, like Femlab, to simulate the partial differential equations describing the optical field in a microtoroid. In addition to mode profiles, it is possible to calculate the mode volume and radiation Q of specific microtoroid resonators. Figure 2.2 is a plot of the fundamental WGM for a 120 μm major diameter and 3 μm minor diameter toroid generated by Femlab.

9

2.2 Microtoroid fabrication

2.2.1 Photolithography and wet etching

Microtoroids are easily fabricated using standard microelectronic fabrication techniques in a process developed by Armani [10]. A diagram showing the fabrication steps is given in Figure 2.4.
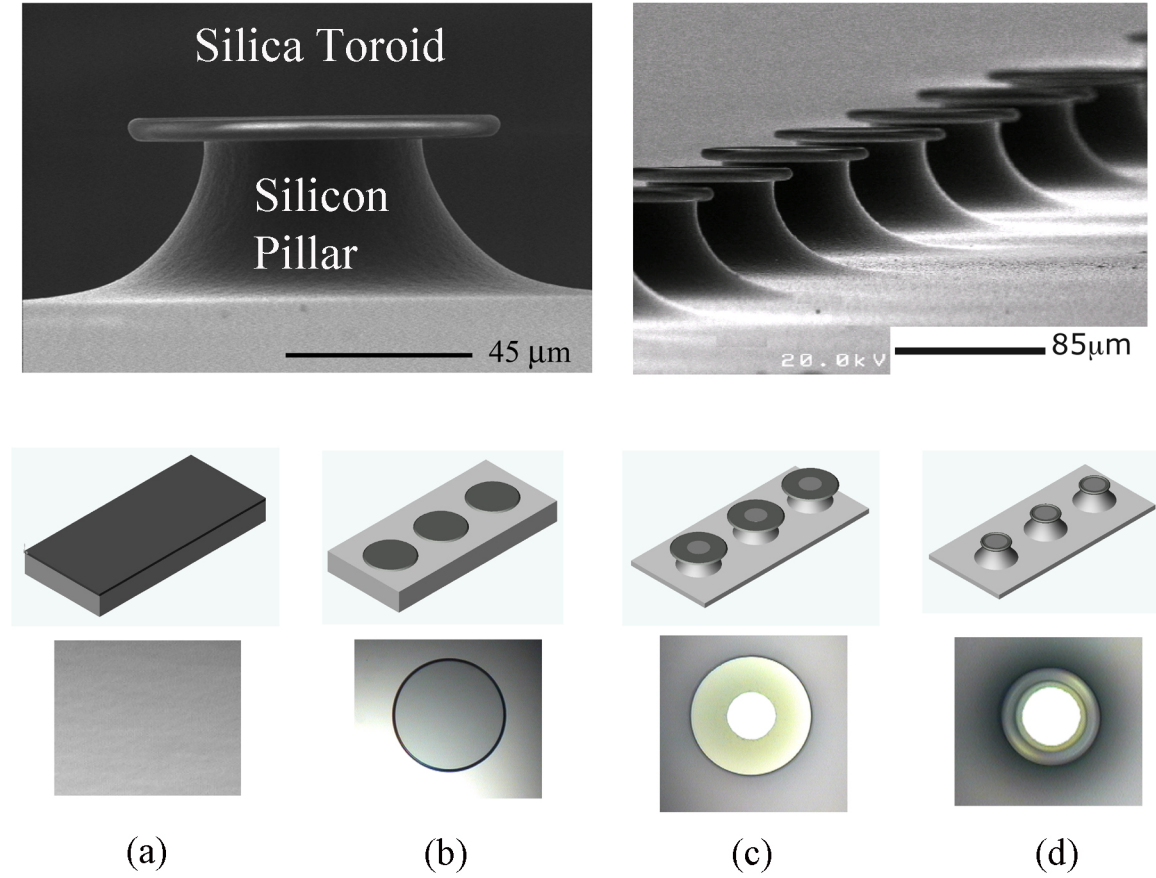

Figure 2.4. Diagram of the fabrication steps of silica microtoroids. (a) First, a photoresist layer is deposited on a SiO_2-on-Si wafer. (b) After photolithography, an HF wet etch creates silica pads. (c) A high-selectivity XeF_2 dry etch isolates silica microdisks from the silicon substrate. (d) Finally, CO_2 laser reflow produces a microtoroid.

First, start with a (100) prime silicon wafer with a 2 μm layer of thermally grown oxide (SiO_2) on top. If necessary, clean the wafer with acetone and isopropyl-alcohol, and dry with nitrogen gas. After the surface is treated with HMDS for 2 minutes to promote surface adhesion, spin coat a uniform layer of Shipley 1813 photoresist onto the wafer at 3,000 rpm. Soft-bake the wafer at 90°C to remove solvents. Next, use a mask aligner (Carl Zuss MJ-BA3) to expose the photoresist with

a mask containing arrays of disks ($40-180\,\mu$m diameter). Stir the exposed wafer in developer until the developing process is complete, normally 30 seconds. For positive resists like S1813, exposed photoresist becomes soluble in developer and is washed away. Left behind are crisp circular pads of photoresist covering the oxide layer. Next, a hard bake is performed at $110°$C to reflow the photoresist pads and prepare for wet etching. The photoresist disk pattern is transferred into the oxide layer by a 19 minute buffered-oxide etch (BOE), in a 2% hydrofluoric acid (HF) solution. The HF etch undercuts the photoresist by a controllable amount, depending on the adhesion strength of resist to the oxide, and any extra etching time added. The HF undercut produces a bevel on the edge of the circular microdisks of the oxide (SiO_2). Normally, this bevel has an angle of $45°$ with respect to the disk plane, but the angle can be reduced to less than $10°$. Small bevel angles are key to high Q in microdisks, which will be discussed in **Chapter 5**.

At this stage in the fabrication, the silica microdisks cannot support whispering-gallery modes because any circulating optical radiation will leak into the higher index silicon substrate. Therefore, a pulsed XeF_2 isotropic dry etch is used, which selectively etches the silicon approximately 1,000 times faster than silica. The etch rate ($\Delta D/\Delta T$) for 4 chips (5×20 mm size) with 100 μm diameter disks is measured to be 0.01 μm per minute for sequential 90 s pulses, depending on the total silicon surface area and pillar diameter. The etch rate is inversely proportional to the pillar diameter as shown in Figure 2.5.
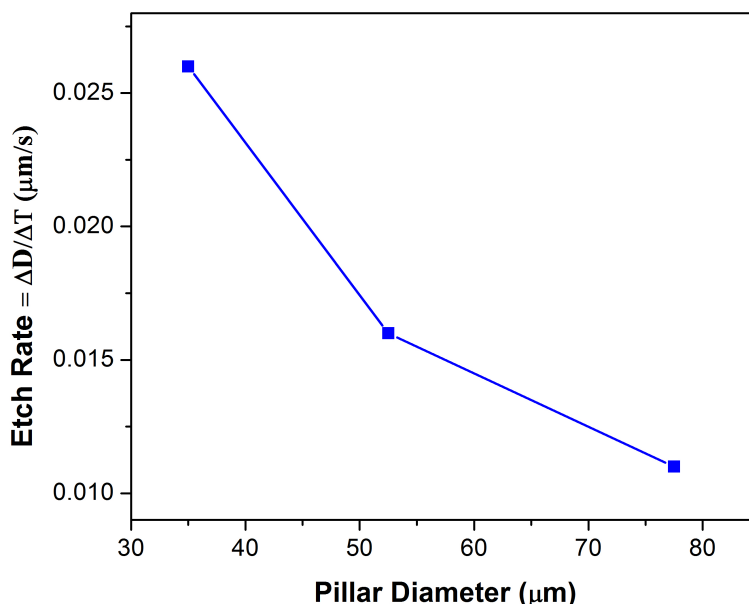

Figure 2.5. Plot of the etch rate of silicon ($\Delta D/\Delta T$) as a function of pillar diameter observed for one microdisk. The etch rate is inversely proportional to the pillar diameter.

The chemical reaction during XeF_2 etching is described by $2XeF_2 + Si \rightarrow 2Xe + SiF_4$. The dry etch should continue until the desired diameter of the silicon pillar is reached, for instance a 40 μm pillar for a 100 μm diameter disk. It is important to note that the silicon chip must be dry before etching. Otherwise, any water on the chip will react with the xenon difluoride gas to produce HF, which etches oxide rapidly and produces surface roughness on the microdisk [37]. After the dry etch, the undercut silica microdisk is supported on a silicon pillar. Microdisks normally have Q factors near 1×10^6, limited by scattering from lithographic and etching roughness. Since the microdisks are fabricated on silicon by standard lithography techniques, they can be easily integrated with other devices on chip, like modulators or detectors.

2.2.2 CO_2 laser reflow

While lasers [9] and plasmonic resonators [29] have been developed using microdisks, the benefits of higher quality factor are well known [38]. Higher Q leads to lower threshold lasers, more sensitive detectors, higher resolution filters, and higher strong coupling coefficients for cQED. After care has been taken to preserve high Q in microdisks by eliminating all contaminants and defects, the quality factor can be increased by an order of magnitude or more by CO_2 laser reflow.

At the CO_2 laser wavelength, 10.6 μm, the absorption cross section of silica is 100 times larger than silicon. Hence, the thermally conductive silicon pillar functions as a circular heat sink, and the silica microdisk is melted to form the toroid geometry. The newly minted glass microtoroid has nearly atomic smooth finish due to surface-tension, like microdroplets [39] and microspheres [6].

A 10 Watt CO_2 laser (Synrad Corp.) is controlled either manually for continuous-wave (cw) power, or by a function generator for pulsing. The author performed laser reflow in three different manners on almost identical microdisks on the same silicon chip to determine the optimum reflow setting. In the first method, the laser is operated in quasi-cw mode, and the laser power is increased steadily until the silica microdisk melts into a microtoroid. In the second method, a single square pulse with 100 ms duration is sent from a function generator to the laser. In the third method, the laser is also controlled with the function generator, but the single 100 ms pulse waveform follows a linearly increasing ramp function. After testing the toroids fabricated according to these three methods, the Q factors were highest for method three. Therefore, the author chose to reflow all microtoroids in the future using the ramp waveform and a single pulse with 100 ms duration. If the laser power (controlled by the peak-to-peak voltage from the function generator) is too low, then the reflow will not be complete and the toroid may be asymmetric. On the other hand, if the laser power is too large, then silicon material can be sputtered onto the toroid and cause absorption loss. For each initial disk diameter and pillar size, there is an optimum reflow power that must be experimentally determined.

2.3 Experimental testing of microtoroids

The standard experimental measurements performed on silica microtoroids for the research presented in this thesis are discussed in detail here. The main elements of toroid testing include: optical excitation of the microcavity by a fiber-coupled tunable laser, coupling of light into and out of the microtoroid with an adiabatic fiber taper, and finally any post-processing of the output light (e.g., wavelength filtering) and optical detection (i.e., conversion from optical to electrical power).

Fiber-coupled semiconductor laser diodes generate optical radiation at 970 nm or 1550 nm for the experiments presented in this work. The lasers are single-frequency and have a bandwidth of less than 300 kHz. The lasers are optically isolated to prevent reflected light from causing laser instability, and the laser is tuned over a wavelength range of more than ten nanometers. Light can be coupled into a microcavity in several ways, including prisms [6], end polished fibers [40], free-space coupling, or fiber tapers [41].

2.3.1 Low-loss optical fiber coupling to microcavities

Tapered optical fibers can excite whispering-gallery resonators with higher efficiency and ideality than any other coupling mechanism [13]. Fiber taper coupling to cavities was first demonstrated with microspheres [42]. Coupling between a taper and any microcavity relies upon the physical overlap and vector phase matching of the evanescent field components of the fiber taper and the microtoroid. With proper phase matching for critical coupling, it is possible to excite the resonator with 100% of the input radiation, made possible by the tapered optical fiber's record ideality (99.999%) [13]. With low transmission loss, low scattering during coupling, and flexible phase-matching, there is no better laboratory tool for probing microcavities than fiber tapers.

2.3.1.1 Fiber taper fabrication

A straight fiber taper is made by pulling a standard single-mode fiber (SMF) at a constant speed (using motors attached to both sides of the fiber) over a hydrogen flame. As the fiber heats up and melts, its diameter is adiabatically reduced until the desired diameter is reached, usually $1-2$ μm. The taper length and final diameter are controlled by adjusting the gas flow rate, the pulling speed, and the flame location. Single-mode tapers can be fabricated with extremely low transmission losses, enabling efficient and ideal coupling to ultra-high Q microtoroids.

Straight fiber tapers are only well phase-matched to a specific microtoroid over a modest wavelength range, roughly 100 nm. For wavelengths outside of this phase-matching range, the optical field phase fronts inside the straight taper is mismatched from the optical field inside the curved resonator. Therefore, the author helped develop a bent fiber taper with a circular twist in the middle [43]. If the radius of curvature of the bent taper fiber matches the microtoroid, coupling is observed
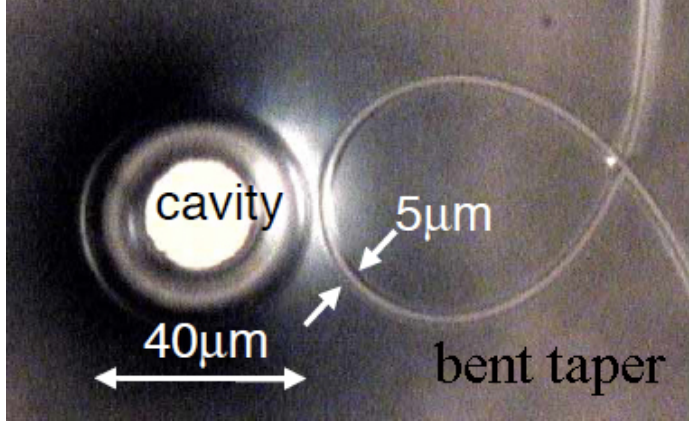
Figure 2.6. Image of a bent fiber taper coupled to a microtoroid. The taper diameter is as small as 5 μm in the center, and the loop diameter is 50 μm.

between the taper and microtoroid over an 900 nm wavelength range from 670 nm to 1570 nm. To make a bent tapered fiber, a straight taper is first pulled from standard SMF. Next, the two sides of the taper are pushed toward one another, forming a circular loop as the taper crosses itself. The fiber positions are carefully controlled to create the desired bent taper diameter, and the loop is frozen into place with gentle heating. The result is a tapered fiber, shown in Figure 2.6 with a circular loop in the center, that can be used to couple optical radiation to a microtoroid over a large bandwidth.

2.3.1.2   Fiber taper phase matching

The taper and toroid must be phase matched to allow efficient optical coupling from one to the other. Therefore, the effective mode indices of the taper (n_{tap}) and toroid (n_{tor}) must be equal. First, the effective mode index of the toroid (n_{tor}) is determined using the previously mentioned finite-element model. Then, the fiber taper mode index is calculated by solving for the propagation constant (β) of light in the fiber. Key physical constants include the fiber core's index of refraction (n), the taper radius (a), and the propagation constant of light $(k_0 = 2\pi/\lambda)$. To simplify the final expression to be solved, several dependent variables can be defined [36].

$$q = \sqrt{\beta^2 - k_0^2}$$
$$h = \sqrt{n^2 k_0^2 - \beta^2}$$
$$\mathrm{R} = \sqrt{-\left(\frac{n^2-1}{2n^2}\right)^2 \left(\frac{\mathrm{K}_2(qa)}{qa \cdot \mathrm{K}_1(qa)}\right)^2 + \left(\frac{\beta}{nk_0}\right)^2 \left(\frac{l}{q^2 a^2} + \frac{1}{h^2 a^2}\right)^2} \qquad (2.11)$$

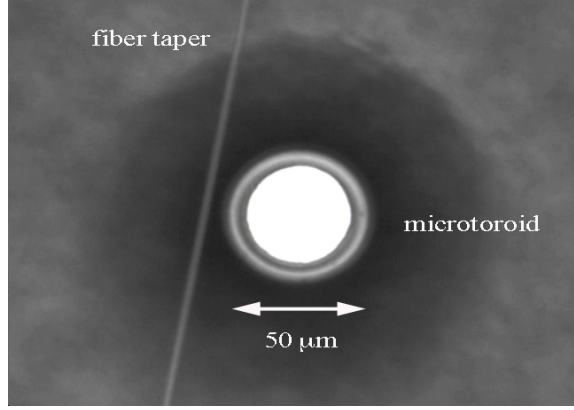After solving the wave equation for the dielectric fiber taper with no cladding, a transcendental

14

Figure 2.7. Top view image showing coupling between a microtoroid ($D = 50$ μm) and fiber taper

equation is derived that can be graphically solved for β, the propagation constant.

$$\frac{\mathrm{J}_0(ha)}{ha \cdot \mathrm{J}_1(ha)} = \frac{1}{h^2 a^2 - \mathrm{R}} - \left(\frac{n^2 + 1}{2n^2}\right)\left(\frac{\mathrm{K}_2(qa)}{qa \cdot \mathrm{K}_1(qa)}\right) \qquad (2.12)$$

After solving for β, the taper mode index is easily calculated as $n_{tap} = \beta/k_0$. To achieve phase matching between the taper and toroid, ensure that $n_{tap} = n_{tor}$. The fiber taper index is matched to the toroid mode by choosing the correct fiber taper radius, a. Normally, the fiber taper is pulled to a minimum diameter less than optimum for phase matching, and the taper position is adjusted with respect to the microtoroid until the phase matched diameter is found. A coupling setup showing the fiber taper waveguide and microtoroid resonator is shown in Figure 2.7.

2.3.2 Quality factor

Silica microcavities can be classified by the optical Q of their WGM resonances—lithographically defined micro-rings ($Q \sim 10^5$), microdisks ($\sim 10^6$), microtoroids ($\sim 10^8$), and microspheres ($\sim 10^9$). The Q factor can be expressed in terms of the linewidth (in frequency or wavelength) of the cavity resonance.

$$Q = \frac{\lambda}{\Delta\lambda} \qquad (2.13)$$

Where $\Delta\lambda$ is the full-width at half-maximum (FWHM) of the resonance lineshape. Or alternatively, the cavity Q can be calculated in terms of the photon lifetime.

$$Q = w\tau \qquad (2.14)$$

These different but equivalent expressions for Q highlight the two methods that can be used to

quantify the intrinsic Q. The first and simplest measurement of cavity Q is quantified in Equation (2.13). This method requires a measurement of the cavity linewidth ($\Delta\lambda$) with the taper and toroid in the undercoupled regime. The injected optical power is kept low ($P < 10\,\mu\text{W}$) to avoid thermal broadening of the cavity linewidth, which will be discussed in Section 2.3.3. To make the measurement, the tunable laser wavelength is linearly scanned at 10 Hz. The taper transmission, which exhibits a dip at the cavity resonance, is measured using a low noise optical detector. Finally, the toroid's resonance lineshape is captured with an oscilloscope, and fit to a Lorenzian function to calculate the width ($\Delta\lambda$) as presented in Figure 2.8. Surface roughness or internal scattering (e.g., index modulation) cause back-scattering in the microtoroid, which splits the previously degenerate cavity resonance into a doublet (two Lorenzian resonances) as shown [44].

If a series of measurements of the linewidth are made and plotted as a function of the taper-toroid gap width, then the intrinsic Q (approached asymptotically) can be calculated by fitting the lineshape. Though the cavity linewidth measurement is the quickest way to estimate Q, this technique is only accurate for cavity linewidths larger than the tunable laser's linewidth (300 kHz). Therefore, the resonance linewidth measurement is only accurate for Q less than 3×10^8.

Alternatively, the toroid intrinsic Q can be accurately determined by a cavity ringdown measurement, a technique that is unaffected by thermal distortion of the cavity linewidth and the laser linewidth. The fiber taper is aligned in critical coupling with the toroid (i.e., $T = 0$) while the laser wavelength is scanned in time like the previous method. At precisely the point when maximum power is coupled into the toroid, the laser excitation is gated off using a high speed, external phase modulator. Afterwards, the taper output power is due entirely to the exponential decay of energy stored in the toroid resonator. The taper output power is recorded in time using a high speed detector and oscilloscope. The cavity lifetime is measured by fitting an exponential to the taper transmission. The result of a cavity ringdown measurement is shown in Figure 2.9. It is important to note that this lifetime for critical coupling (τ_{cc}) is smaller than the intrinsic lifetime (τ_0) due to cavity loaded by the fiber taper. To calculate the intrinsic Q factor, it is necessary to account for taper loading and back-scattering in the resonator that couples the clockwise and counterclockwise modes.

The frequency splitting ($2\gamma^{-1}$) between the doublet modes is proportional to the amount of back-scattering. With measurements of the loaded lifetime and splitting, the intrinsic Q can be calculated using the following equation.

$$Q_0 = w\tau_0 = \frac{2w}{\tau_{crit}\left(\frac{1}{\tau_{crit}^2} - \frac{1}{\gamma^2}\right)} \tag{2.15}$$

The record microtoroid Quality factor is currently 4×10^8, observed by Tobias Kippenberg in a $70\,\mu\text{m}$ toroid [12]. The author's research into the upper limit of Q factor in microtoroids is discussed
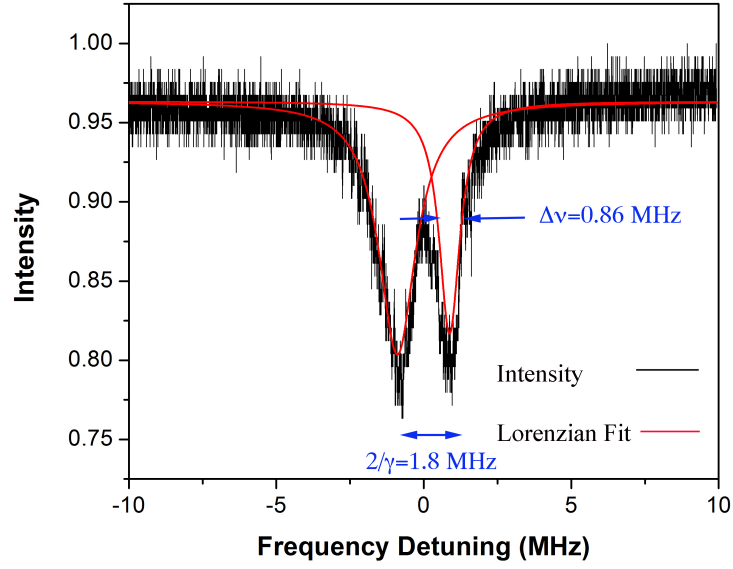
16

Figure 2.8. Plot of the taper transmission versus laser detuning frequency, showing a characteristic doublet mode of a microtoroid ($D = 55$ μm). The resonance lineshape of each mode (black) is fit to a Lorenzian (red). The sub MHz linewidth ($\Delta\nu$) of one resonance and the splitting frequency (γ^{-1}) are also marked.
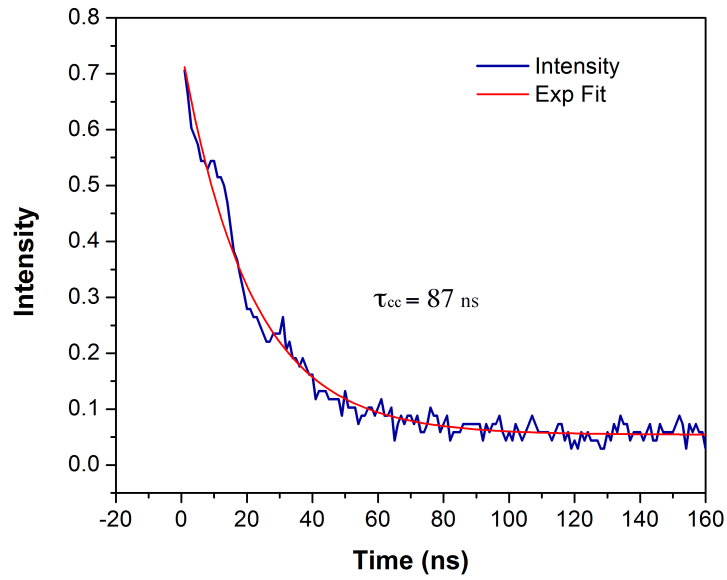

Figure 2.9. Plot of the power emitted from a critically coupled microtoroid during cavity ringdown measurement. The cavity output is recorded after the input is gated off by a modulator. The intensity decay in time is fit to an exponential, and the cavity ringdown lifetime (τ_{cc}) at critical coupling is calculated.

17

in **Chapter 6**.

2.3.3 Thermal broadening

Microtoroids exhibit thermal broadening of ultra-high Q resonances for moderate input powers due to the low thermal conductivity of silica and the toroid's small mode volume. Resonant buildup of cavity energy can create large amounts of circulating power. For instance, 1 mW of input power critically coupled into a microtoroid with $Q = 1 \times 10^8$ can produce 100 W of circulating power (see Equation (2.16))! For a 50 μm diameter toroid, 100 W of internal power corresponds to a circulating intensity of 1 GW/cm^2, sufficient to observe many nonlinear phenomena.

$$P_{circ} = \left(\frac{4\lambda Q_0}{9\pi^2 nD} \right) P_{in} \tag{2.16}$$

The temperature of the microtoroid cavity will increase with such a large amount of power is circulating inside the glass. As a result, the microtoroid's resonance location will red-shift (towards longer wavelengths), due to the positive thermal coefficient of the refractive index of silica ($\frac{dn}{dT} = 1.3 \times 10^{-5} K^{-1}$) [45]. Also, the thermal expansion coefficient of silica ($\alpha_T = 5.5 \times 10^{-7}$) induces a smaller red-shift of the resonance location.

The normal red-shift of the cavity resonance is illustrated in Figure 2.10, where the normal Lorenzian lineshape has broadened into a triangle. The broadening occurs as the laser wavelength is swept upwards in time, shown by the plot of the laser piezo voltage. The laser wavelength is linearly increased in time, and as the taper-cavity coupling approaches critical coupling, the circulating power in the toroid increases linearly. As a result, the resonance location moves towards longer wavelengths, lengthening the amount of time required to reach critical coupling and thereby broadening the resonance. At critical coupling, the cavity power is maximum, and therefore the resonance location cannot move further. Finally, the laser wavelength (still increasing in time) moves past the cavity's shifted resonance wavelength, and the taper transmission snaps quickly back to 100%. But, when the laser wavelength is scanned downwards in time (shown on the left side of Figure 2.10), the cavity resonance width is artificially compressed as the resonance red-shifts against the blue-tuning laser. In summary, the positive thermal coefficients (thermal and expansion) of silica at room temperature cause thermal broadening of the resonance when the pump wavelength is tuned upwards, and contraction for negative tuning. A helpful review of the thermal effects in silica microtoroids has been written by Carmon [46].
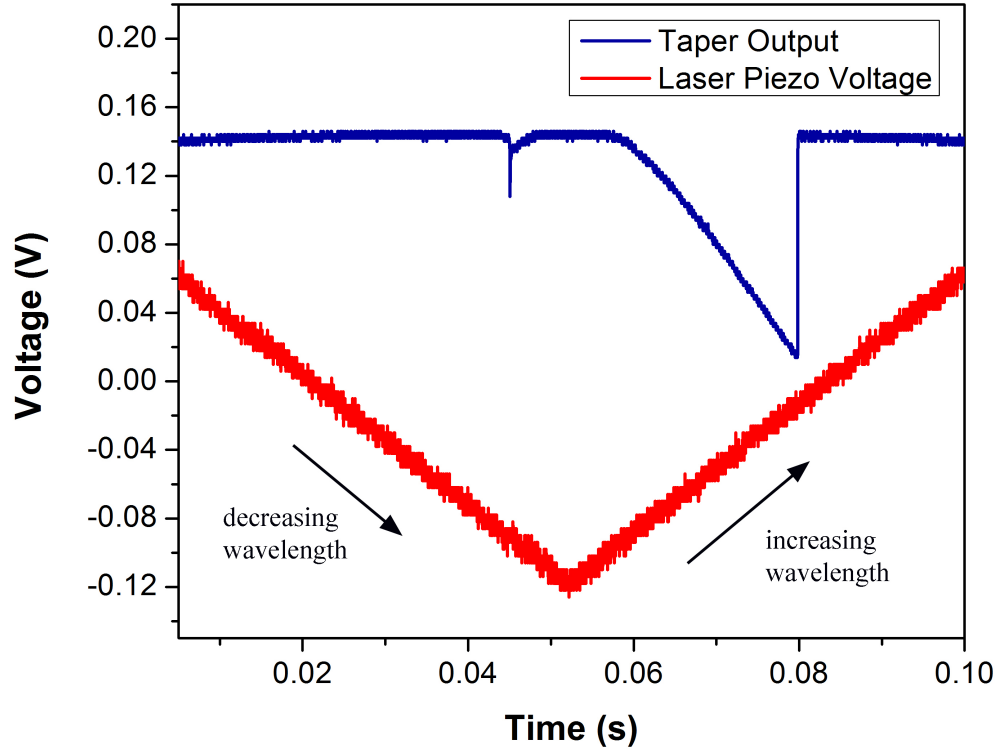
Figure 2.10. Plot of the taper transmission in time (shown in blue) and the laser piezo voltage (shown in red) when critically coupled to a microtoroid exhibiting thermal broadening due to $+\delta n/\delta T$. The normal Lorenzian mode is broadened when the laser wavelength is increased in time (positive slope for laser piezo−right side), and the resonance is narrowed in time when the laser wavelength is swept downwards (negative slope for laser piezo−left side).

2.3.4 Inverse thermal broadening

Thermal broadening can be exploited to stabilize the taper and toroid coupling. If the laser frequency is detuned to the blue-shifted side of the broadened resonance (left side of triangle), then any perturbations such as temperature, coupling, or frequency jitter of the laser will be compensated by the thermal effect. However, blue-shifted photons (lower wavelength) cause heating of the toroid mode. If the total thermal coefficient of silica could be made negative, then a pump laser could be stabilized on the red-side of a toroid cavity resonance, which would cool the toroid mode. Laser cooling of microcavities is very important, for it would aid researchers in reaching the quantum mechanical ground state of a macroscopic object [47]. Kippenberg has demonstrated side-band resolved cooling of a microtoroid, using a state-of-the-art feedback system for stabilizing the laser wavelength on the red-side of the cavity resonance [48].

The author has successfully demonstrated stabilized laser coupling on the red-side of a microtoroid resonance. The thermal coefficient of refractive index of the cavity mode was changed from positive to negative with a thin polymer coating. Polymethyl Methacrylate (PMMA) has a negative thermal coefficient of refractive index ($\frac{dn}{dT} = -1.2 \times 10^{-4}\mathrm{C}^{-1}$) [49], however its optical loss ($\alpha = 23\,\mathrm{m}^{-1}$) is greater than silica's at $\lambda = 1550\ \mu\mathrm{m}$ [50]. To demonstrate a microtoroid with negative thermal broadening, a high Q microtoroid was first tested and its Q factor recorded ($Q_0 = 1 \times 10^7$). Then, a drop of 4% PMMA polymer was applied to the microtoroid, and the microtoroid was spun at 2,000 rpm for 30 seconds, resulting in a 0.4 μm thick PMMA coating on the toroid. The silicon chip, on which the silica toroid resides, was baked at 170°C for 10 minutes to cure the polymer. Finally, the thermal broadening characteristics of the polymer coated toroid were measured using a tunable laser, and the final Q was measured to be 4×10^5, which is 25 times lower than the Q before coating. Figure 2.11 demonstrates that the cavity mode thermal coefficient is now slightly negative, since the thermal broadening occurs when the the laser wavelength is scanned downwards (left side). As the power stored in the microtoroid resonator increases, the resonance wavelength blue-shifts to lower wavelengths. With this novel microcavity, a pump laser can be stabilized on the red-shifted side of the cavity mode, which in turn can cool the microtoroid mode.

Following the author's work, a colleague showed a similar effect for a microtoroid coated with PDMS. The final Q factor (1.5×10^6) is higher than for PMMA due to the lower absorption coefficient of PDMS ($\alpha = 4\,\mathrm{m}^{-1}$) [51]. However, any polymer coating will reduce the Q of the microtoroid since its loss cannot match that of silica, possibly limiting the application of this technique. Future experiments can study the use of other thin film materials (e.g., Cytop, $\alpha = 0.2\,\mathrm{m}^{-1}$) with lower absorption loss [50].
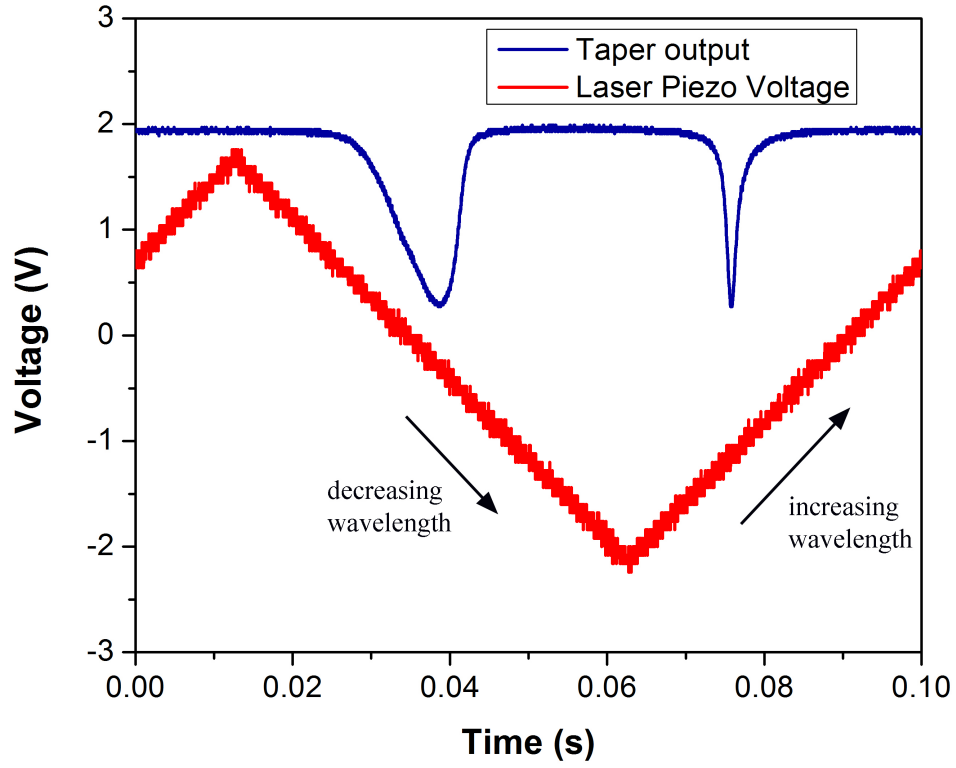
Figure 2.11. Plot of the taper transmission in time (shown in blue) and the laser piezo voltage (shown in red) when critically coupled to a microtoroid exhibiting inverse thermal broadening due to the cavity mode's effective $-\delta n/\delta T$. The normal Lorenzian resonance broadens in time when the laser wavelength is swept downwards in time−negative slope for laser piezo, and the resonance narrows when the laser wavelength is decreased in time−positive slope for laser piezo.

2.4　Summary

In this chapter, the ultra-high Q microtoroid resonator was discussed. Microtoroid's have extremely low cavity loss and ultra-small mode volumes, making them unique resonators with applications in low-threshold lasers and nonlinear optics to name just a few. The whispering-gallery mode structure of microtoroids was analyzed with a finite element model. The evanescent field component of WGMs is an important element of the work presented in this thesis, and enables long duration and efficient interaction of optical radiation with different environments.

Also, the fabrication process for creating optical microtoroids was discussed. Microtoroids can be made quickly and inexpensively on silicon. The selective laser reflow of microdisks into microtoroids endows them with ultra high quality factors. The experimental testing of microtoroids was described, including fiber taper coupling. Finally, the thermal broadening effect in silica microtoroids was investigated. The author coated microtoroids with a polymer to change the sign of the thermo-optical coefficient, which made stable coupling on the red-shifted side of cavity resonance possible.